



## RESEARCH LETTER

10.1029/2018GL081794

Impulsive Source of the 2017  $M_W = 7.3$  Ezgeleh, Iran, Earthquake

## Key Points:

- The Ezgeleh earthquake ruptured a flat thrust fault in the Zagros fold and thrust belt
- Kinematic slip modeling reveals a highly impulsive source with southward directivity, possibly causing the large damage in the area
- The direction of coseismic slip suggests a strain partitioning between thrust and unmapped strike-slip faults

## Supporting Information:

- Supporting Information S1
- Movie S1
- Movie S2

## Correspondence to:

B. Gombert,  
baptiste.gombert@earth.ox.ac.uk

## Citation:

Gombert, B., Duputel, Z., Shabani, E., Rivera, L., Jolivet, R., & Hollingsworth, J. (2019). Impulsive source of the 2017  $M_W = 7.3$  Ezgeleh, Iran, earthquake. *Geophysical Research Letters*, 46. <https://doi.org/10.1029/2018GL081794>

Received 21 DEC 2018

Accepted 30 APR 2019

Accepted article online 8 MAY 2019

B. Gombert<sup>1,2</sup> , Z. Duputel<sup>2</sup> , E. Shabani<sup>3</sup> , L. Rivera<sup>2</sup> , R. Jolivet<sup>4</sup> ,  
and J. Hollingsworth<sup>5</sup>

<sup>1</sup>Department of Earth Sciences, University of Oxford, Oxford, UK, <sup>2</sup>Institut de Physique du Globe de Strasbourg, UMR7516, Université de Strasbourg, EOST/CNRS, Strasbourg, France, <sup>3</sup>Department of Seismology, Institute of Geophysics, University of Tehran, Tehran, Iran, <sup>4</sup>Laboratoire de géologie, Département de Géosciences, École Normale Supérieure, PSL Research University, CNRS UMR 8538, Paris, France, <sup>5</sup>ISTerre/CNRS, UMR5275, Université Grenoble Alpes, Grenoble, France

**Abstract** On 12 November 2017, a  $M_W = 7.3$  earthquake struck near the Iranian town of Ezgeleh, at the Iran-Iraq border. This event was located within the Zagros fold and thrust belt which delimits the continental collision between the Arabian and Eurasian Plates. Despite a high seismic risk, the seismogenic behavior of the complex network of active faults is not well documented in this area due to the long recurrence interval of large earthquakes. In this study, we jointly invert interferometric synthetic aperture radar and near-field strong motions to infer a kinematic slip model of the rupture. The incorporation of these near-field observations enables a fine resolution of the kinematic rupture process. It reveals an impulsive seismic source with a strong southward rupture directivity, consistent with significant damage south of the epicenter. We also show that the slip direction does not match plate convergence, implying that some of the accumulated strain must be partitioned onto other faults.

**Plain Language Summary** Iran is a very seismically active region. However, the 2017 Ezgeleh earthquake of magnitude 7.3 occurred in a region where large earthquakes have not been documented for several centuries. Our knowledge of fault locations, geometries, and seismic behaviors is therefore limited in this region. We use near-field seismological and satellite geodetic data to retrieve the spatial and temporal distribution of slip occurring on the fault during the Ezgeleh earthquake. We show that the high slip rate and Southward directivity of the rupture may have worsened the damage south of the epicenter. We also observe that tectonic motion is partitioned between different types of faults. Although the Ezgeleh earthquake did release a significant part of that strain, other seismogenic faults in the region could represent an important hazard for the nearby population.

## 1. Introduction

On 12 November 2017, the Iranian province of Kermanshah and the Iraqi Kurdistan were shaken by a severe  $M_W = 7.3$  earthquake located south of the border. It caused the death of ~630 people and considerable damage, in particular in the Iranian city of Sarpol-e Zahab (cf. Figure 1). The earthquake triggered numerous landslides and rock falls, including a massive 4 × 1-km landslide in Kermanshah (Miyajima et al., 2018).

The hypocenter is located within the Zagros Mountains near the Iranian town of Ezgeleh, a tectonically active region that accommodates crustal shortening (e.g., Berberian & King, 1981) resulting from the collision between the Arabian Plate and the Eurasian Plate. About a third to a half of current convergence is accommodated within the Zagros belt (Vernant et al., 2004). The belt hosts many moderate earthquakes ( $M = 5-6$ ) with depths ranging from 4 to 20 km, although this range is debated (e.g., Niazi et al., 1978; Nissen et al., 2011; Talebian & Jackson, 2004). Our knowledge of the regional seismotectonics is further complicated by the very rare occurrence of coseismic surface rupture (Talebian & Jackson, 2004; Walker et al., 2005).

The Ezgeleh earthquake occurred at the transition between the Lorestan Arc in the southeast and the Kirkuk Embayment (KE) in the northwest (cf. Figure 1). The area is covered by an 8- to 13-km-thick sedimentary cover heavily folded into numerous anticlines (e.g., Alavi, 2007; Falcon, 1969). Sediments are crossed by many thrust faults that flatten within the basement (Sadeghi & Yassaghi, 2016; Tavani et al., 2018). As

©2019. The Authors.

This is an open access article under the terms of the Creative Commons Attribution-NonCommercial-NoDerivs License, which permits use and distribution in any medium, provided the original work is properly cited, the use is non-commercial and no modifications or adaptations are made.

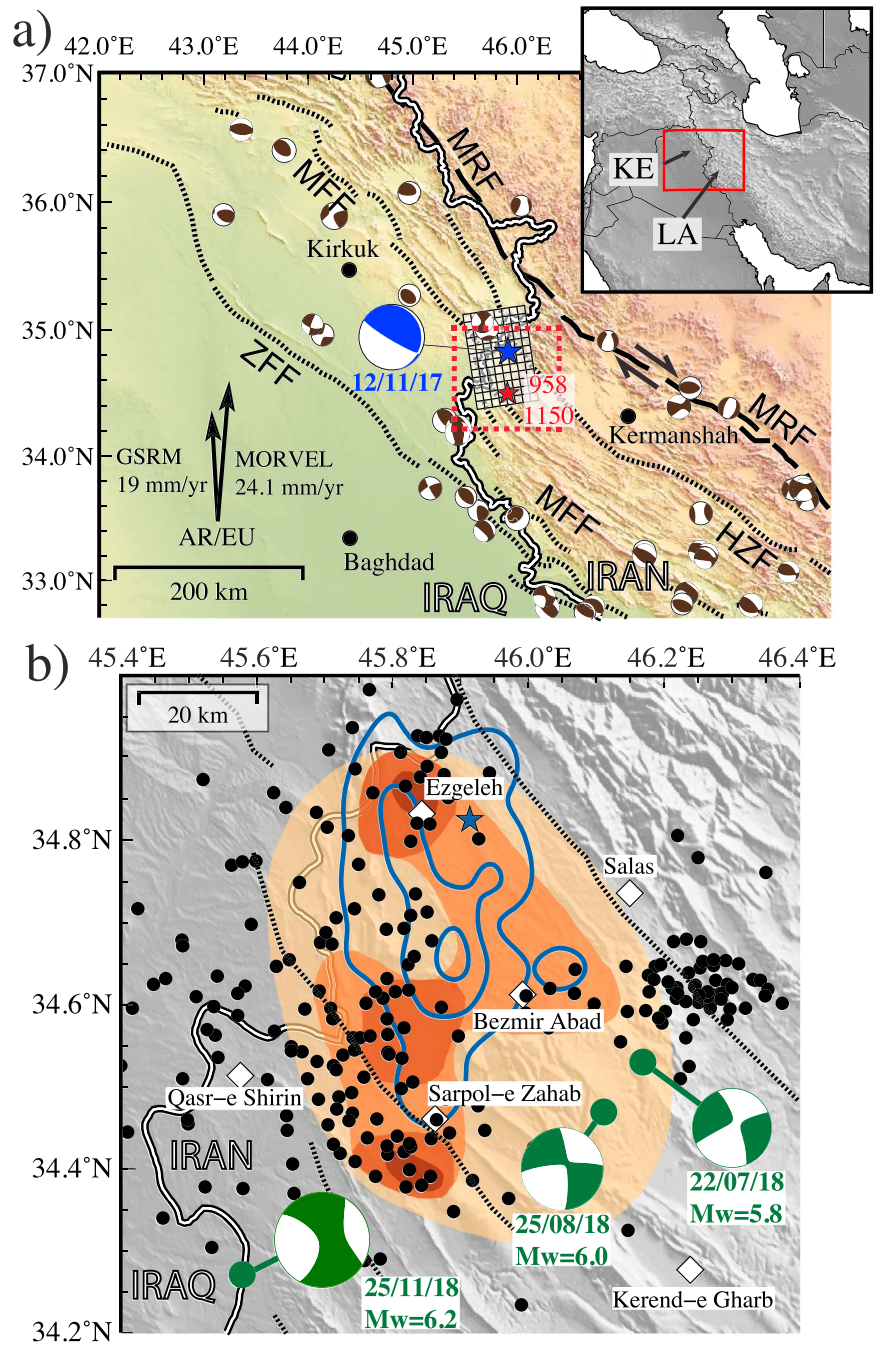


**Figure 1.** Regional seismotectonic context and damage associated with the 2017 Ezgeleh earthquake. (a) The blue star marks the epicenter location, and the squares represent the fault parametrization. The blue beachball is the moment tensor estimated in this study, and the brown moment tensors are regional seismicity from the Global CMT catalog (Ekström et al., 2012). The red star shows the approximate location of two historical earthquakes. The dashed black line is the Main Recent Fault (MRF), and dotted lines are supposed locations of regional blind faults (MFF = Mountain Flexure Fault; HZF = High Zagros Fault; ZFF = Zagros Foredeep Fault; Berberian, 1995). Arrows indicate the convergence of the Arabian plate (AR) with respect to stable Eurasia (EU) from the GSRM v2.1 (Kreemer et al., 2014) and MORVEL (DeMets et al., 2010) models, computed with the UNAVCO Plate Motion Calculator. LA = Lorestan Arc. KE = Kirkuk Embayment. The red dashed square indicates the position of (b). (b) Black dots are aftershocks located by the International Institute of Earthquake Engineering and Seismology of Iran. Focal mechanisms from the Global CMT catalog of three large aftershocks are shown in green. Brown colors indicate the level of damage based on a compilation of destruction rate and landslide activity interpolated from field surveys conducted by the Geological Survey of Iran (GSI, 2017). The darker the color, the more intense the damage. Blue lines are the 1.5-m coseismic slip contour. CMT = centroid moment tensor.

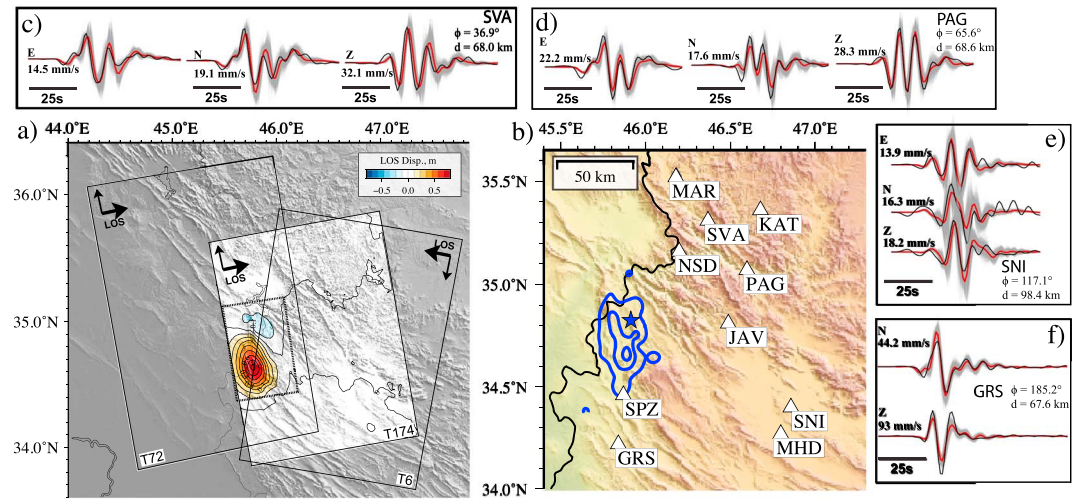


**Figure 2.** Observations used in the inversion. (a) Unwrapped Sentinel-1A interferograms showing surface displacement in Line Of Sight (LOS) direction (Track 174). The footprint of one additional ascending and descending tracks are also shown. Data, predictions, and model performance of the three interferograms are available in Figures S1 and S2. (b) Location of strong-motion records (white triangles). (c–f) Waveforms of four selected stations around the epicenter. For each waveform, the bold number indicates its maximum amplitude.  $\Phi$  and  $d$  are station azimuth and distance to epicenter, respectively. The black line is the recorded waveform, gray lines are stochastic predictions for our posterior model, and the red line is the mean of stochastic predictions. Remaining waveforms are shown in Figure S3.

expected from the lack of surface ruptures and fault scarps, most of these faults are blind, hence the difficulty to infer their geometry. In this region, plate convergence is roughly north-south (cf. Figure 1) with a rate between 19 (Kreemer et al., 2014) and 24 mm/year (DeMets et al., 2010). Slip is partitioned between thrust faults at the front of the belt, such as the Mountain Front Fault, the High Zagros Fault, the Zagros Foredeep Fault, and the Main Recent Fault, a right lateral strike-slip fault located at the back of the belt (cf. Figure 1; Berberian, 1995). This part of the Zagros belt hosts moderate seismicity, but the last significant earthquakes ( $5.9 \lesssim M \lesssim 6.4$ ) to strike the area happened in 958 and 1150 (Ambraseys & Melville, 2005). Therefore, our understanding of the regional seismotectonic setting is obscured by the undersampled seismic cycle and the absence of ground geodesy. The 2017 Ezgeleh earthquake highlighted the seismic hazard in this portion of the Zagros belt. Its analysis hence provides a unique opportunity to enrich our understanding of the region and the associated seismic hazard. In addition, the availability of near-field strong-motion records offers the possibility to closely study the propagation of the rupture on the fault.

In this study, we propose a stochastic analysis of the 2017 earthquake source process. We use a Bayesian framework to infer a population of coseismic slip models that fit available observations. While currently available studies were either limited to the static final distribution of slip on the fault (Barnhart et al., 2018; He et al., 2018; Vajedian et al., 2018; Wanpeng et al., 2018; Yang et al., 2018) or used far-field teleseismic data (Chen et al., 2018; Nissen et al., 2019), we jointly invert interferometric synthetic aperture radar (InSAR) and near-field strong-motion data which provide a better resolution (Anderson, 2003) to propose a kinematic description of the earthquake source. We use a layered velocity model that is routinely used to locate earthquakes by the Iranian Seismological Center, which ensures modeling is performed to the best of our knowledge (supporting information Table S1).

## 2. Inversion of Coseismic Slip

### 2.1. Observations

Due to the remote location of the event, the only available geodetic data come from InSAR. We use three synthetic aperture radar interferograms computed from acquisition by the Sentinel-1 satellite, along two ascending and one descending tracks (Figures 2a, S1, and S2). We use the ISCE software with precise orbits and Shuttle Radar Topography Mission Digital Elevation Model (DEM) to compute the coseismic interferograms (Rosen et al., 2012). The coherence of the radar phase is excellent, likely due to the arid conditions of this region. Acquisition dates are available in Table S2. We measure up to 80 cm of ground displacement toward the satellite in the ascending tracks, suggesting uplift and/or displacement toward the southwest.

The number of data points in the unwrapped interferograms is reduced using a recursive quad tree algorithm (cf., Figure S1; Lohman & Simons, 2005). We estimate uncertainties due to tropospheric perturbations in the phase by estimating empirical covariance functions for each interferogram (Jolivet et al., 2014). Estimated covariance parameters are summarized in Table S2.

We include near-field seismic waveforms recorded by 10 strong-motion accelerometers from the Iran Strong Motion Network to constrain the temporal evolution of slip during the earthquake rupture. Although located only on one side of the rupture, all stations are within 102 km of the epicenter (cf. Figure 2b). Details on strong motion data processing are given in supporting information Text S1 (Ide, 2007; Lee & Lahr, 1972). The east component of the two stations located south of the rupture (SPZ and GRS) was not used due to the poor quality of the record. We integrate accelerometric data to recover ground velocity, downsampled to 1 sps. Waveforms are bandpass filtered between 7 and 50 s using a fourth-order Butterworth band-pass filter, then windowed around the first arrivals.

## 2.2. Estimation of the Fault Plane

The two nodal planes of the global centroid moment tensor mechanism (Ekström et al., 2005) are either a shallow northeast dipping plane (351° strike and 11° dip) or a nearly vertical plane (121° strike and 83° dip). We conduct a grid search on fault geometry parameters for each nodal plane. The goal is to discriminate between the two planes and to find the optimal fault geometry to limit forward modeling errors.

We grid search the fault location and its strike and dip angles by inverting the InSAR displacement to find the geometry that better explains the observations. For each tested geometry, slip is inverted on 96 subfault patches using a simple least squares technique. More details on the method are given in supporting information Text S2 (Tarantola, 2005). We find that even the best subvertical plane has a root-mean-square 6 times larger than the shallow-dipping plane (cf. Figures S4 and S5). Although the subvertical plane is compatible with a back thrust fault that may exist in the region (Tavani et al., 2018) or with the reactivation of steep normal faults (Jackson, 1980), the shallow-dipping plane is in better agreement with receiver functions analysis (Paul et al., 2010) and the tectonic setting (e.g., Berberian, 1995; Vergés et al., 2011). Our optimal plane (351° strike, 14° dip, 13-km depth) agrees well with other studies using a similar grid search approach (Barnhart et al., 2018; Wanpeng et al., 2018). In the following, we will consider that the Ezgeleh earthquake occurred on our optimum shallow dipping plane.

## 2.3. Coseismic Slip Modeling

We use fault parameters inferred in section 2.2 to construct a planar fault and divide it into 96 subfault patches, each with a dimension of  $7 \times 7$  km<sup>2</sup>. Patch size was determined through trial and error to limit correlation between slip on neighboring parts of the fault. Source model parameters include total final slip, rupture velocity, and rise time for each patch along with hypocenter location. We define  $\mathbf{m}_S$  the vector including the two components of static slip (i.e., final integrated slip), and  $\mathbf{m}_K$  the vector of kinematic parameters describing the temporal evolution of slip.

We solve the problem in a Bayesian framework using AlTar, a Markov chain Monte Carlo algorithm based on the algorithm described by Minson et al. (2013). It samples the full posterior probability distribution of the models that fit observations and are consistent with prior information. The strength of our solution is that it does not rely on any spatial smoothing and provides accurate estimates of the posterior slip uncertainty. We sample the posterior probability density  $p(\mathbf{m}_S, \mathbf{m}_K | \mathbf{d}_S, \mathbf{d}_K)$  given by

$$p(\mathbf{m}_S, \mathbf{m}_K | \mathbf{d}_S, \mathbf{d}_K) \propto p(\mathbf{m}_K) p(\mathbf{m}_S) p(\mathbf{d}_S | \mathbf{m}_S) p(\mathbf{d}_K | \mathbf{m}_S, \mathbf{m}_K) \quad (1)$$

where  $\mathbf{d}_S$  and  $\mathbf{d}_K$  are the InSAR and strong-motion observations, respectively. The prior PDFs  $p(\mathbf{m}_S)$  and  $p(\mathbf{m}_K)$  are mostly uniform distributions designed to prevent some model features such as back slip. They are described in detail in Table S3. For further details on the method, the reader can refer to supporting information Text S3 (Duputel et al., 2014; Herrmann, 2013; Minson et al., 2013) and Gombert et al. (2018).

## 3. Results

In the first seconds following the hypocentral time, slip propagates in every direction around the hypocenter (cf. Figure 3 and supporting information Movie S1). Approximately 5 s after origin, the rupture almost only propagates toward the south. The largest slip rate occurs roughly after 6 s, 20 km south of the epicenter. We observe a strong directivity toward the south, consistent with a shorter, higher amplitude signal at stations

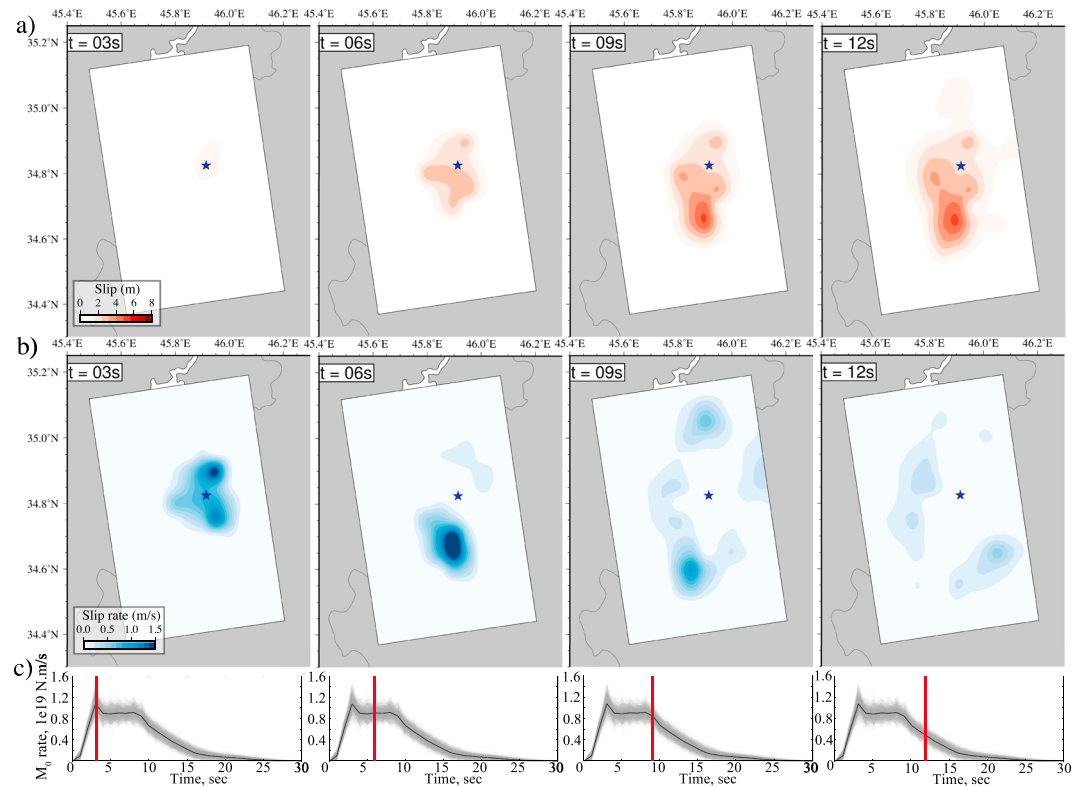


**Figure 3.** Temporal evolution of coseismic slip. (a) Cumulative slip on the fault 3, 6, 9, and 12 s after the origin time. The red color scale indicates slip amplitude. (b) Evolution of slip rate on the fault. (c) Source time function (STF) of the event. Gray lines are stochastic STF models inferred from our model population, while the black curve represents the posterior mean STF. Vertical red lines indicate the time of each snapshot.

SPZ and GRS compared to stations located in the north (cf. Figures 2 and S3). In addition, we infer a large slip rate on the fault. As shown in Figures 4d, 4e, and S6, slip rate increases up to more than 3 m/s where the slip is maximum. The slip rate functions of two fault patches presented here show the fast increase in slip rate associated with a short rise time  $\leq 5$  s, defining a sharp slip pulse (Heaton, 1990). Although larger than the values usually reported in kinematic slip models (usually ranging from 0.1 to 1 m/s), our slip rate estimates for this event are compatible with well-documented earthquakes (e.g., Cirella et al., 2012; Minson et al., 2014). The fast slip rate of the fault is reflected in the moment rate function shown in Figure 3c. To obtain the moment rate function, we first calculate the scalar moment function,  $M_0(t)$ , by summing the moment tensor function of each subfault and using the definition of the scalar moment from Dahlen and Tromp (1998). The moment rate function is then obtained using the time derivative of  $M_0(t)$ . As shown in Figure 3c, 90% of the moment was released within the first 14 s of the rupture, depicting an overall impulsive earthquake. The mean rupture speed along strike is  $3.0 \pm 0.25$  km/s (Figure S7), which is  $\sim 0.9V_s$  at that depth.

The posterior mean model of the final cumulative slip is shown in Figure 4a. At first order, this solution is in agreement with previously published static models (Barnhart et al., 2018; Wanpeng et al., 2018). We infer a  $\sim 50$ -km-long and  $\sim 30$ -km-wide rupture, with a peak slip of  $5.5 \pm 0.5$  m. One difference arises as previous models proposed that two distinct asperities ruptured during the earthquake. Our posterior mean model does not show a clearly distinct rupture area in the north, closer to the hypocenter. However, roughly 20% of the models in our solution present such a feature (see supporting information Movie S2). This indicates that it is in the realm of possibilities but available observations cannot entirely resolve it. The slip direction is constant along most of the fault, with a  $131.5^\circ \pm 0.8^\circ$  rake corresponding to a motion toward the southwest. The inferred focal mechanism is therefore consistent with long-period moment tensor inversions.

Our Bayesian framework allows us to directly infer the posterior uncertainties associated with the model parameters. Slip uncertainties are represented in Figure 4a by the 95% confidence ellipses. In addition, pos-

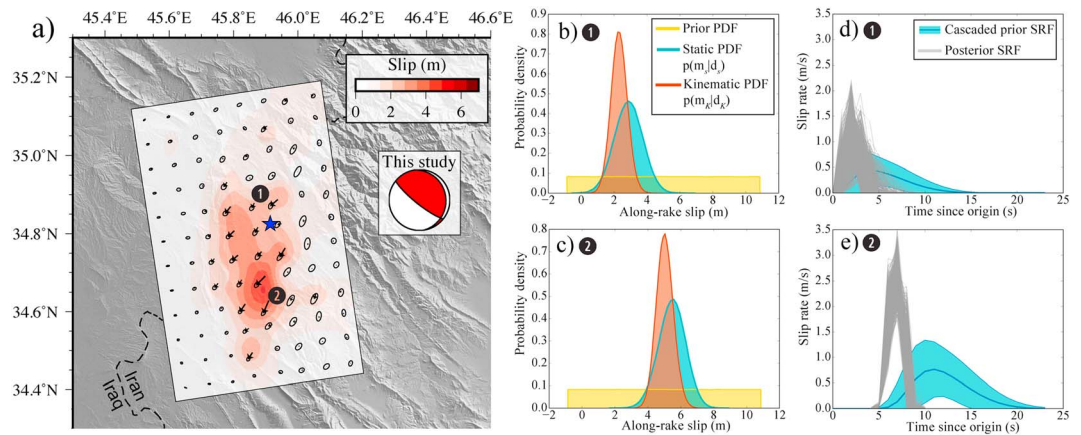


**Figure 4.** Final coseismic slip distribution. (a) Color and arrows on the fault plane indicate amplitude and direction of slip, respectively. Ellipses represent the 95% posterior uncertainty. Results presented in subfigures (b–e) are obtained for patches labeled 1 and 2. The background topography comes from the Shuttle Radar Topography Mission (Farr et al., 2007). (b, c) Prior, posterior static PDF, and posterior kinematic PDF of along-rake slip in patches 1 and 2. (d, e) Slip rate evolution in patches 1 and 2. The blue line is the mean prior slip rate function (SRF) used in the sampling, surrounded by  $1\sigma$  uncertainties. Posterior SRFs in gray are from 1000 models randomly selected from our solution.

terior marginal distributions after the static and kinematic inversions of the along-rake slip of two fault patches are shown in Figures 4b and 4c. Unsurprisingly, the inclusion of kinematic observations reduces the posterior uncertainties of those parameters. On the highest slipping patch for instance, the  $1\sigma$  posterior uncertainty decreases from 0.82 to 0.52 m. Over the fault, we observe a rather low posterior uncertainty at shallow and intermediate depths, where slip is located. At depths larger than 15 km, uncertainties become more significant. However, the inspection of each model composing the solution reveals a good consistency in the slip distribution, with nonetheless a larger variability in the northern part of the rupture (cf. supporting information Movie S2). This is confirmed by our analysis of the model ensemble revealing that data provide more information where the fault experienced large slip (cf. supporting information Text S4 and Figure S8).

As shown in Figures S1, S2, and S9, model predictions fit Sentinel-1A observations very well. Residuals are small over the three tracks, and they are consistent with the amplitude of 5–7 days of postseismic signal ( $\sim 10$  cm; Barnhart et al., 2018). Stochastic model predictions of the strong-motion data are shown in Figures 2 and S3. Overall, our solution can explain the observations with a good accuracy. Posterior model predictions of stations KAT, SNI, and MHD suffer from larger uncertainties, likely explained by their greater distance from the hypocenter.

#### 4. Discussion

As suggested by previous studies (Barnhart et al., 2018; He et al., 2018; Wanpeng et al., 2018), the Ezgeleh earthquake likely occurred on the Mountain Flexure Fault (sometimes referred to as Main Front Fault, noted MFF in Figure 1). Along the major part of the Zagros belt, the MFF follows a NW-SE axis with a  $\sim 120^\circ$  azimuth and is aligned with many topographic features (visible on the DEM in Figure 4). However, the strike of the fault differs by about  $50^\circ$  with the topography orientation at the location of the earthquake. This discrepancy is explained by a major bend in the MFF at this location as it transitions between the Lorestan Arc in the south and the KE in the north (e.g., Koshnaw et al., 2017; Vergés et al., 2011). Interestingly, the fault bend between the Lorestan Arc and KE corresponds to the northern bound of the rupture (Figure 3). This geometry change possibly stopped the rupture propagation, as suggested by numerical models (Aochi et al., 2000). The rupture may also have been halted by the 8- to 10-km-thick sediment cover, whose depth roughly corresponds to the updip limit of slip. Although poorly constrained, these boundaries could nonetheless help to better assess the probable size for future large events in the region, a valuable element in seismic hazard assessment (e.g., Hetényi et al., 2016).

These sediments are heavily folded in the forearc basin and host many large anticlines (e.g., Casciello et al., 2009; Kent, 2010). These folds are evidence for thin-skin shortening occurring within the belt (Koshnaw

et al., 2017). However, the slip of the 2017 earthquake occurred at larger depth, between 10 and 15 km. This deeper coseismic deformation suggests that thick-skin shortening is also happening in this part of the Zagros range (Nissen et al., 2011; Vergés et al., 2011). The slip direction of the Ezgeleh earthquake on the MFF is nearly perpendicular to the alignment of the topographic features mentioned above (cf. Figure 4a), creating a maximum 65 cm of uplift and 33 cm of subsidence across the belt (cf. Figure S10). Despite the relatively large depth of the Ezgeleh earthquake, such coseismic deformation may thus contribute to the growth of the Zagros topography. Afterslip might also contribute, although it seems to occur on a shallow dipping decollement at the front of the mountain range (Barnhart et al., 2018).

An interesting feature of the Ezgeleh earthquake is the discrepancy between the coseismic slip direction and the current plate motion. Both the GSRM v2.1 model (Kreemer et al., 2014) and the MORVEL model (DeMets et al., 2010) predict a nearly N-S plate convergence (see Figure 1), while the overall coseismic slip vector is oriented on a S 30°W axis (see Figure 4).

This difference suggests that strain partitioning is occurring in this part of the Zagros belt, with a partial decoupling between the thrust and right lateral strike-slip motion (McCaffrey, 1992; Platt, 1993). Strain partitioning in the Lurestan Arc and the KE has been proposed before based on the analysis of regional focal mechanisms (Talebian & Jackson, 2004). The Main Recent Fault (MRF; see Figure 1) is a major NW-SE, 800-km-long right lateral strike-slip fault which accommodates some of the strain (Tchalenko & Braud, 1974). It hosted several large earthquakes and has an ~50-km horizontal offset (Talebian & Jackson, 2002). However, other structures may be accommodating the strike-slip component of the convergence. Between July and November 2018, three significant aftershocks with respective magnitudes of  $M_w = 5.8$ ,  $M_w = 6.0$ , and  $M_w = 6.2$  occurred south of the mainshock epicenter (cf. Figure 1b). These events present a right lateral strike-slip focal mechanism but are located more than 100 km west of the MRF. They could have ruptured the Khanaqin fault, a N-S strike-slip structure marking the boundary between the Lurestan Arc and the KE (e.g., Blanc et al., 2003; Berberian, 1995; Hessami et al., 2001). However, there is very limited evidence that the Khanaqin fault is actually a strike-slip fault. As a matter of fact, a recent study by Tavani et al. (2018) using reconstruction of seismic profiles proposed that the Khanaqin fault is a back thrust structure accommodating the SW-NE motion. Therefore, undetected strike-slip faults may be accommodating some of the strike-slip deformation closer to the forearc than the MRF. Throughout the Zagros, the MRF is known to accommodate a major component of the northward motion via strain partitioning (Talebian & Jackson, 2002). However, not all the regional shear is accommodated solely on the MRF, especially along its northwest limit, where strike-slip faulting becomes increasingly distributed (Copley & Jackson, 2006). The additional contribution from other less known active structures in this region therefore poses an important uncharacterized seismic risk for local populations.

While the rupture directivity imaged here is visible in published slip models (Chen et al., 2018; Nissen et al., 2019), the sharpness of the slip pulse in these studies is blurred by their use of far-field data and smoothing constraints. The good spatial and temporal resolution of our kinematic slip model enabled by the use of near-field observations reveals interesting features. Figures 3 and S6 show that the rupture starts as a growing crack that rapidly transition into a pulse with a rise time of about 4 s. This crack-pulse transition occurs within the first 4 s and less than 7 km from the hypocenter, therefore away from the rupture boundaries. Day (1982) proposed that if the slip rate is controlled by the fault geometry the rise time should be  $T_R = 0.5 \times W/V_R$ , with  $W$  the fault width and  $V_R$  the rupture velocity. However, we infer  $T_R$  values systematically higher than inverted rise times (Figure S11). This pulse-like behavior is therefore unlikely to result from healing phases emanating from the along-dip finiteness of the fault. A rapid crack-pulse transition is in agreement with early observations by Heaton (1990) and later studies (e.g., Beroza & Mikumo, 1996; Meier et al., 2016; Wang et al., 2019). Such a pulse may result from a number of mechanisms such as frictional self-healing, fault strength or stress heterogeneities, bimaterial effects, and wave reflections within low-velocity fault zones (e.g., Andrews & Ben-Zion, 1997; Huang & Ampuero, 2011; Perrin et al., 1995). After this early transition from a growing crack, the rupture continues its journey along strike as a decaying pulse toward the north and a strong growing pulse toward the south.

This strong southward propagating pulse seems to have a significant impact in the distribution of damage and landslides triggered by the earthquake. The Ezgeleh earthquake induced extensive destructions of dwellings in Iraqi Kurdistan, but mostly in the Iranian province of Kermanshah. Figure 1b shows the intensity of damage created by the mainshock. It is obtained from field observations conducted by the Inter-

national Institute of Earthquake Engineering and Seismology of Iran. Reported macroseismic intensities are also shown in Figure S12. Damage intensity roughly follows the surface projection of the slip distribution, but larger damage was reported in the south. In addition to building damage, many rockfalls and landslides occurred south of the rupture and up to 125 km from the centroid, including a large 4-km-long and 1-km-wide landslide (Miyajima et al., 2018). These observations may however be biased by the difficulty to report such phenomena on the Iraqi side of the border. Many different factors can also largely influence the effects of an earthquake, like soil nature or mountain slopes. In addition to rupture directivity, studies have suggested that the strong impulsiveness of the source can intensify low-frequency ground shaking, particularly damaging to buildings (Melgar & Hayes, 2017; Somerville & Graves, 2003). The large slip rate and short rise time of the southward propagating pulse may therefore have exacerbated the damage observed southwest of the Ezgeleh earthquake.

## 5. Conclusion

The 2017 Ezgeleh earthquake breaks a long hiatus on strong events affecting the Zagros thrust and fold belt in the Kermanshah province. The joint inversion of InSAR and near-field strong-motion observations reveals a predominantly thrust motion on a near-horizontal blind crustal fault. We also infer a highly impulsive source propagating toward the south. These kinematic properties may have played a role in the numerous slope instabilities and in the important damage that affected Iranian cities.

Furthermore, the misalignment between the plate convergence and the slip direction provide additional hints for a strain partitioning in this part of the Zagros belt between thrust motion on flat crustal faults and right lateral strike slip. As suggested by late aftershocks, unmapped dextral faults could be accommodating part of that shear strain and therefore represent an important seismic risk for nearby populations.

## References

### Acknowledgments

This project has received funding from the European Research Council (ERC) under the European Union's Horizon 2020 research and innovation program under grant agreements 758210 and 805256. This work also received financial support from Agence Nationale de la Recherche (project ANR-17-ERC3-0010). The Copernicus Sentinel-1 data were provided by the European Space Agency (ESA). Seismological observations belong to the Iran Strong Motion Network (<https://ismn.bhrc.ac.ir/en>). We acknowledge the Geological Survey of Iran (Seismotectonics and Seismology group) for making available their preliminary report (in Persian). It can be obtained upon request to [info@gsi.ir](mailto:info@gsi.ir). The AlTar algorithm used for the inversion was developed by the Seismological Laboratory at Caltech and was provided by Mark Simons. We thank the Editor, Gavin Hayes, and two anonymous reviewers for their constructive comments which helped improve this manuscript.

- Alavi, M. (2007). Structures of the Zagros fold-thrust belt in Iran. *American Journal of Science*, 307(9), 1064–1095.
- Ambraseys, N. N., & Melville, C. P. (2005). *A history of Persian earthquakes*. Cambridge, UK: Cambridge University Press.
- Anderson, J. G. (2003). Strong-motion seismology. *International Geophysics Series*, 81(B), 937–966.
- Andrews, D. J., & Ben-Zion, Y. (1997). Wrinkle-like slip pulse on a fault between different materials. *Journal of Geophysical Research*, 102(B1), 553–571.
- Aochi, H., Fukuyama, E., & Matura, M. (2000). Spontaneous rupture propagation on a non-planar fault in 3-D elastic medium. *Pure and Applied Geophysics*, 157(11-12), 2003–2027.
- Barnhart, W. D., Brengman, C. M. J., Li, S., & Peterson, K. E. (2018). Ramp-flat basement structures of the Zagros Mountains inferred from co-seismic slip and afterslip of the 2017  $M_w$  7.3 Darbandikhan, Iran/Iraq earthquake. *Earth and Planetary Science Letters*, 496, 96–107.
- Berberian, M. (1995). Master blind thrust faults hidden under the Zagros folds: Active basement tectonics and surface morphotectonics. *Tectonophysics*, 241(3-4), 193–224.
- Berberian, M., & King, G. C. P. (1981). Towards a paleogeography and tectonic evolution of Iran. *Canadian Journal of Earth Sciences*, 18(2), 210–265.
- Beroza, G. C., & Mikumo, T. (1996). Short slip duration in dynamic rupture in the presence of heterogeneous fault properties. *Journal of Geophysical Research*, 101(B10), 22,449–22,460.
- Blanc, E.-P., Allen, M. B., Inger, S., & Hassani, H. (2003). Structural styles in the Zagros simple folded zone, Iran. *Journal of the Geological Society*, 160(3), 401–412.
- Casciello, E., Vergés, J., Saura, E., Casini, G., Fernández, N., Blanc, E., et al. (2009). Fold patterns and multilayer rheology of the Lurestan Province, Zagros simply folded belt (Iran). *Journal of the Geological Society*, 166(5), 947–959.
- Chen, K., Xu, W., Mai, P. M., Gao, H., Zhang, L., & Ding, X. (2018). The 2017  $M_w$  7.3 Sarpol Zahāb earthquake, Iran: A compact blind shallow-dipping thrust event in the mountain front fault basement. *Tectonophysics*, 747, 108–114.
- Cirella, A., Piatanesi, A., Tinti, E., Chini, M., & Cocco, M. (2012). Complexity of the rupture process during the 2009 L'Aquila, Italy, earthquake. *Geophysical Journal International*, 190(1), 607–621.
- Copley, A., & Jackson, J. (2006). Active tectonics of the Turkish-Iranian plateau. *Tectonics*, 25, TC6006. <https://doi.org/10.1029/2005TC001906>
- Dahlen, F. A., & Tromp, J. (1998). *Theoretical global seismology*. Princeton, NJ: Princeton University Press.
- Day, S. M. (1982). Three-dimensional finite difference simulation of fault dynamics: Rectangular faults with fixed rupture velocity. *Bulletin of the Seismological Society of America*, 72(3), 705–727.
- DeMets, C., Gordon, R. G., & Argus, D. F. (2010). Geologically current plate motions. *Geophysical Journal International*, 181(1), 1–80.
- Duputel, Z., Agram, P. S., Simons, M., Minson, S. E., & Beck, J. L. (2014). Accounting for prediction uncertainty when inferring subsurface fault slip. *Geophysical Journal International*, 197(1), 464–482.
- Ekström, G., Dziewonski, A. M., Maternovskaya, N. N., & Nettles, M. (2005). Global seismicity of 2003: Centroid–moment-tensor solutions for 1087 earthquakes. *Physics of the Earth and Planetary Interiors*, 148(2-4), 327–351.
- Ekström, G., Nettles, M., & Dziewonski, A. M. (2012). The global CMT project 2004–2010: Centroid-moment tensors for 13,017 earthquakes, 200–201, 1–9.
- Falcon, N. L. (1969). Problems of the relationship between surface structure and deep displacements illustrated by the Zagros Range. *Geological Society, London, Special Publications*, 3(1), 9–21.
- Farr, T. G., Rosen, P. A., Caro, E., Crippen, R., Duren, R., Hensley, S., et al. (2007). The shuttle radar topography mission. *Reviews of Geophysics*, 45, RG2004. <https://doi.org/10.1029/2005RG000183>

- GSI (2017). Preliminary report on geological features of the Ezgaleh-Kermanshah earthquake ( $M$  7.3), November 12, 2017, West Iran. GSI preliminary report number: 17-01, ver.03.
- Gombert, B., Duputel, Z., Jolivet, R., Simons, M., Jiang, J., Liang, C., et al. (2018). Strain budget of the Ecuador–Colombia subduction zone: A stochastic view. *Earth and Planetary Science Letters*, *498*, 288–299.
- He, P., Wen, Y., Xu, C., & Chen, Y. (2018). High-quality three-dimensional displacement fields from new-generation SAR imagery: Application to the 2017 Ezgeleh, Iran, earthquake. *Journal of Geodesy*, *93*, 573–591.
- Heaton, T. H. (1990). Evidence for and implications of self-healing pulses of slip in earthquake rupture. *Physics of the Earth and Planetary Interiors*, *64*(1), 1–20.
- Herrmann, R. B. (2013). Computer programs in seismology: An evolving tool for instruction and research. *Seismological Research Letters*, *84*(6), 1081–1088.
- Hessami, K., Koyi, H., & Talbot, C. J. (2001). The significance of strike-slip faulting in the basement of the Zagros fold and thrust belt. *Journal of Petroleum Geology*, *24*(1), 5–28.
- Hetényi, G., Cattin, R., Berthet, T., Le Moigne, N., Chopel, J., Lechmann, S., et al. (2016). Segmentation of the Himalayas as revealed by arc-parallel gravity anomalies. *Scientific reports*, *6*, 33866.
- Huang, Y., & Ampuero, J.-P. (2011). Pulse-like ruptures induced by low-velocity fault zones. *Journal of Geophysical Research*, *116*, B12307. <https://doi.org/10.1029/2011JB008684>
- Ide, S. (2007). Slip inversion, *Treatise on geophysics* (Vol. 4, pp. 193–224). Amsterdam: Elsevier.
- Jackson, J. (1980). Reactivation of basement faults and crustal shortening in orogenic belts. *Nature*, *283*(5745), 343–346.
- Jolivet, R., Duputel, Z., Riel, B., Simons, M., Rivera, L., Minson, S., et al. (2014). The 2013  $M_w$  7.7 Balochistan earthquake: Seismic potential of an accretionary wedge. *Bulletin of the Seismological Society of America*, *104*(2), 1020–1030.
- Kent, W. N. (2010). Structures of the Kirkuk Embayment, northern Iraq: Foreland structures or Zagros Fold Belt structures. *GeoArabia*, *15*(4), 147–188.
- Koshnaw, R. I., Horton, B. K., Stockli, D. F., Barber, D. E., Tamar-Agha, M. Y., & Kendall, J. J. (2017). Neogene shortening and exhumation of the Zagros fold-thrust belt and foreland basin in the Kurdistan region of northern Iraq. *Tectonophysics*, *694*, 332–355.
- Kreemer, C., Blewitt, G., & Klein, E. C. (2014). A geodetic plate motion and Global Strain Rate Model. *Geochemistry, Geophysics, Geosystems*, *15*, 3849–3889. <https://doi.org/10.1002/2014GC005407>
- Lee, W. H. K., & Lahr, J. C. (1972). HYPO71: A computer program for determining hypocenter, magnitude, and first motion pattern of local earthquakes. US Geological Survey.
- Lohman, R. B., & Simons, M. (2005). Some thoughts on the use of InSAR data to constrain models of surface deformation: Noise structure and data downsampling. *Geochemistry, Geophysics, Geosystems*, *6*, Q01007. <https://doi.org/10.1029/2004GC000841>
- McCaffrey, R. (1992). Oblique plate convergence, slip vectors, and forearc deformation. *Journal of Geophysical Research*, *97*(B6), 8905–8915.
- Meier, M.-A., Heaton, T., & Clinton, J. (2016). Evidence for universal earthquake rupture initiation behavior. *Geophysical Research Letters*, *43*, 7991–7996. <https://doi.org/10.1002/2016GL070081>
- Melgar, D., & Hayes, G. P. (2017). Systematic observations of the slip pulse properties of large earthquake ruptures. *Geophysical Research Letters*, *44*, 9691–9698. <https://doi.org/10.1002/2017GL074916>
- Minson, S., Simons, M., & Beck, J. (2013). Bayesian inversion for finite fault earthquake source models I—Theory and algorithm. *Geophysical Journal International*, *194*(3), 1701–1726.
- Minson, S., Simons, M., Beck, J., Ortega, F., Jiang, J., Owen, S., et al. (2014). Bayesian inversion for finite fault earthquake source models—II: The 2011 great Tohoku-oki, Japan earthquake. *Geophysical Journal International*, *198*(2), 922–940.
- Miyajima, M., Fallahi, A., Ikemoto, T., Samaei, M., Karimzadeh, S., Setiawan, H., et al. (2018). Site investigation of the Sarpole-Zahab earthquake,  $M_w$  7.3 in SW Iran of November 12, 2017. *JSCSE Journal of Disaster, FactSheet*: FS2018-E-0002.
- Niazi, M., Asudeh, I., Ballard, G., Jackson, J., King, G., & McKenzie, D. (1978). The depth of seismicity in the Kermanshah region of the Zagros Mountains (Iran). *Earth and Planetary Science Letters*, *40*(2), 270–274.
- Nissen, E., Ghods, A., Karasözen, E., Elliott, J. R., Barnhart, W. D., Bergman, E. A., et al. (2019). The 12 November 2017  $M_w$  7.3 Ezgeleh–Sarpol-zahab (Iran) earthquake and active tectonics of the Lurestan arc. *Journal of Geophysical Research: Solid Earth*.
- Nissen, E., Tatar, M., Jackson, J. A., & Allen, M. B. (2011). New views on earthquake faulting in the Zagros fold-and-thrust belt of Iran. *Geophysical Journal International*, *186*(3), 928–944.
- Paul, A., Hatzfeld, D., Kaviani, A., Tatar, M., & Péquegnat, C. (2010). Seismic imaging of the lithospheric structure of the Zagros Mountain belt (Iran). *Geological Society, London, Special Publications*, *330*(1), 5–18.
- Perrin, G., Rice, J. R., & Zheng, G. (1995). Self-healing slip pulse on a frictional surface. *Journal of the Mechanics and Physics of Solids*, *43*(9), 1461–1495.
- Platt, J. (1993). Mechanics of oblique convergence. *Journal of Geophysical Research*, *98*(B9), 16,239–16,256.
- Rosen, P. A., Gurrola, E., Sacco, G. F., & Zebker, H. (2012). The InSAR scientific computing environment. In *VDE, 2012. EUSAR. 9th European Conference on Synthetic Aperture Radar* (pp. 730–733).
- Sadeghi, S., & Yassaghi, A. (2016). Spatial evolution of Zagros collision zone in Kurdistan, NW Iran: Constraints on Arabia–Eurasia oblique convergence. *Solid Earth*, *7*(2), 659–659.
- Somerville, P., & Graves, R. (2003). Characterization of earthquake strong ground motion. *Landslide tsunamis: Recent findings and research directions*, Springer pp. 1811–1828.
- Talebian, M., & Jackson, J. (2002). Offset on the Main Recent Fault of NW Iran and implications for the late Cenozoic tectonics of the Arabia–Eurasia collision zone. *Geophysical Journal International*, *150*(2), 422–439.
- Talebian, M., & Jackson, J. (2004). A reappraisal of earthquake focal mechanisms and active shortening in the Zagros Mountains of Iran. *Geophysical Journal International*, *156*(3), 506–526.
- Tarantola, A. (2005). Inverse problem theory and methods for model parameter estimation. *Siam* 89.
- Tavani, S., Parente, M., Puzone, F., Corradetti, A., Gharabegli, G., Valinejad, M., et al. (2018). The seismogenic fault system of the 2017  $M_w$  7.3 Iran–Iraq earthquake: Constraints from surface and subsurface data, cross-section balancing, and restoration. *Solid Earth*, *9*(3), 821.
- Tchalenko, J., & Braud, J. (1974). Seismicity and structure of the Zagros (Iran): The Main Recent Fault between 33 and 35°N. *Philosophical Transactions of the Royal Society A*, *277*(1262), 1–25.
- Vajedian, S., Motagh, M., Mousavi, Z., Motaghi, K., Fielding, E., Akbari, B., et al. (2018). Coseismic deformation field of the  $M_w$  7.3 12 November 2017 Sarpole-Zahab (Iran) earthquake: A decoupling horizon in the northern Zagros Mountains inferred from InSAR observations. *Remote Sensing*, *10*(10), 1589.
- Vergés, J., Saura, E., Casciello, E., Fernandez, M., Villaseñor, A., Jiménez-Munt, I., & García-Castellanos, D. (2011). Crustal-scale cross-sections across the NW Zagros belt: Implications for the Arabian margin reconstruction. *Geological Magazine*, *148*(5-6), 739–761.

- Vernant, P., Nilforoushan, F., Hatzfeld, D., Abbassi, M., Vigny, C., Masson, F., et al. (2004). Present-day crustal deformation and plate kinematics in the Middle East constrained by GPS measurements in Iran and northern Oman. *Geophysical Journal International*, *157*(1), 381–398.
- Walker, R. T., Andalibi, M., Gheitanchi, M., Jackson, J., Karegar, S., & Priestley, K. (2005). Seismological and field observations from the 1990 November 6 Furg (Hormozgan) earthquake: A rare case of surface rupture in the Zagros Mountains of Iran. *Geophysical Journal International*, *163*(2), 567–579.
- Wang, Y., Day, S. M., & Denolle, M. A. (2019). Geometric controls on pulse-like rupture in a dynamic model of the 2015 Gorkha earthquake. *Journal of Geophysical Research: Solid Earth*, *124*, 1544–1568. <https://doi.org/10.1029/2018JB016602>
- Wanpeng, F., Sergey, S., Rafael, A., Ali, Y., Junhua, L., Qiang, Q., et al. (2018). Geodetic constraints of the 2017  $M_w$  7.3 Sarpol Zahab, Iran earthquake and its implications on the structure and mechanics of the north-west Zagros thrust-fold belt. *Geophysical Research Letters*, *45*, 6853–6861. <https://doi.org/10.1029/2018GL078577>
- Yang, Y.-H., Hu, J.-C., Yassaghi, A., Tsai, M.-C., Zare, M., Chen, Q., et al. (2018). Midcrustal Thrusting and Vertical Deformation Partitioning Constraint by 2017  $M_w$  7.3 Sarpol Zahab earthquake in Zagros Mountain belt, Iran. *Seismological Research Letters*, *89*(6), 2204–2213.